Lab on a Chip

Using Airflow-Driven, Evaporative Gradients to Improve Sensitivity and Fluid Control in Colorimetric Paper-Based Assays

Journal:	*Lab on a Chip*
Manuscript ID	LC-ART-06-2021-000542.R1
Article Type:	Paper
Date Submitted by the Author:	20-Sep-2021
Complete List of Authors:	Wang, Edward; University of California San Diego, Mechanical and Aerospace Engineering Guo, Zhilin; University of California San Diego, Mechanical and Aerospace Engineering Tang, Rui; University of California San Diego, Electrical and Computer Engineering Lo, Yu-Hwa; University of California, Department of Electrical and Computer Engineering

Using Airflow-Driven, Evaporative Gradients to Improve Sensitivity and Fluid Control in Colorimetric Paper-Based Assays†

Edward Wang[a], Zhilin Guo[a], Rui Tang[b] and Yu-Hwa Lo[ab]

a) Department of Aerospace and Mechanical Engineering, Materials Science and Engineering Program, UC-San Diego, San Diego, USA
b) Department of Electrical and Computer Engineering, UC-San Diego, San Diego, USA

† Electronic supplementary information (ESI) available

Abstract

Microfluidic paper-based analytical devices (uPADs) are foundational devices for point-of-care testing, yet suffer from limitations in regards to their sensitivity and capability in handling complex assays. Here, we demonstrate an airflow-based, evaporative method that is capable of manipulating fluid flows within paper membranes to offer new functionalities for multistep delivery of reagents and improve the sensitivity of uPADs by 100-1000 times. This method applies an air-jet to a pre-wetted membrane, generating an evaporative gradient such that any solutes become enriched underneath the air-jet spot. By controlling the lateral position of this spot, the solutes in the paper strip are enriched and follow the air jet trajectory, driving the reactions and enhancing visualization for colorimetric readout in multistep assays. The technique has been successfully applied to drive the sequential delivery in multistep immunoassays as well as improve sensitivity for colorimetric detection assays for nucleic acids and proteins via loop-mediated isothermal amplification (LAMP) and ELISA. For colorimetric LAMP detection of the COVID-19 genome, enrichment of the solution on paper could enhance the contrast of the dye in order to more clearly distinguish between the positive and negative results to achieve a sensitivity of 3 copies of SARS-Cov-2 RNAs. For ELISA, enrichment of the oxidized TMB substrate yielded a sensitivity increase of two-to-three orders of magnitude when compared to non-enriched samples – having a limit of detection of around 200 fM for IgG. Therefore, this enrichment method represents a simple process that can be easily integrated into existing detection assays for controlling fluid flows and improving detection of biomarkers on paper.

1. Introduction

Microfluidic paper-based analytical devices (uPADs) have long been established as an attractive area for point-of-care testing (POCT)[1,2]. These devices use paper as the key platform in the fabrication of various diagnostic assays. Paper, comprised primarily of cellulose fibers, presents an inexpensive and lightweight material which is beneficial for overall cost reduction. In addition, the presence of cellulose fibers allows the capability of wicking liquids via capillary action, thereby allowing simple operation without the use of external pumps[3]. These advantages coupled with the biocompatibility and flexibility in diagnosing a variety of biomarkers have accelerated the growth of these devices as diagnostic tools.

Within this field, one of the most prominent readout methods for uPADs has been through colorimetric means[4,5]. In colorimetric assays, detection of a biomarker is accompanied by a color change which is often proportional to the amount of biomarker present. Color change can be induced by various detection chemistries such as small-molecule organic indicators[6,7], metal nanoparticles[8–10], and chromogenic enzyme reactions[10–12]. While the results can be either qualitative or quantitative, colorimetric assays represent a significant portion of current uPAD research due to their user-friendly nature.

Despite this abundance of research in colorimetric detection, these assays suffer from key limitations which have slowed down its commercialization. The frontmost of these issues remains in their poor sensitivity, having detection limits orders of magnitudes lower than those performed by clinical instruments[13]. Sensitivity issues are often attributed to the inhomogeneous distribution of the colorimetric substance and the presence of background noise generated by either the paper or sample itself. Various methods to resolve these issues within colorimetric assays have been proposed. Here, novel means of color generation and amplification have been the most widely studied alternatives. These include the use of enzyme-nanoparticle conjugates[14], hybridized metallic and organic nanoparticles[15–17], and enhanced metallic nanoparticle staining[18,19] which act to further increase color development and subsequent contrast.

In addition to poor sensitivity, lack of fluid control in rudimentary uPADs has restricted their use to single reaction type assays[20]. As paper based ELISAs are typically more complex and require the stepwise delivery of various reagents, multiple mechanisms of fluid flow control have been explored. Within this field, two categories of techniques have emerged - passive and active means of fluid control[21]. Generally, passive methods manipulate fluid flow through physical restructuring or chemical treatment of the device. These include the use of dissolvable solutes[22,23], creation of physical valves [24–27], and geometric adjustments[28,29]. While passive methods are advantageous regarding ease of fabrication, design simplicity, and expandability, they have limitations in fluid manipulation as the speed and direction of fluid flow is determined by pre-set elements in the device. Conversely, active methods aim to control fluid flow with the incorporation of external inputs. Using mechanical actuation[30–32] and geometric transformations[33–35], various types of switches and valves have been designed to manage fluid flow speed, direction, or entry. Based on their programmable nature, active methods can therefore offer a higher degree of flexibility and more precise control over fluids.

While the limitations regarding immunoassay sensitivity and fluid control have been subject to numerous studies, these two issues remain somewhat exclusive as the rationale to improve these constraints is either to increase the limit of detection or for integration into multistep assays, respectively. In this paper we present an active, airflow-based enrichment method that can control the fluid flow and improve sensitivity for paper-based colorimetric assays. This method is accomplished by aiming an airflow nozzle perpendicular to a pre-wetted membrane. A differential evaporative gradient is induced as the area immediately underneath the airflow experiences a higher evaporation rate than the rest of the membrane. Due to the formation of this gradient, the surrounding liquid will migrate towards the spot in order to replenish the lost water. During this process, the replenishing water will carry any dissolved molecules towards this area such that they will be concentrated underneath the nozzle. While solute

enrichment occurs while the airflow source is stationary, fluid control and sequential delivery can be achieved by dynamic airflow positioning across the filter surface.

We demonstrate the simplicity and flexibility of the airflow enrichment method through its applications in colorimetric, paper-based protein and nucleic acid detection. Specifically, we used paper-based ELISA and isothermal RT-LAMP as these assays show the most potential for being integrated into widespread POCT devices. For protein detection, evaporative-induced fluid control was incorporated into a multistep immunoassay as a delay valve and switch to demonstrate the sequential delivery of specific reagents. In addition, the airflow enrichment of the colorimetric substrate generated in ELISA and isothermal RT-LAMP could be focused on a single spot to improve sensitivity and visualization without the need for alternative systems of color generation.

2. Results and Discussion

2.1 Theoretical basis for evaporative enrichment

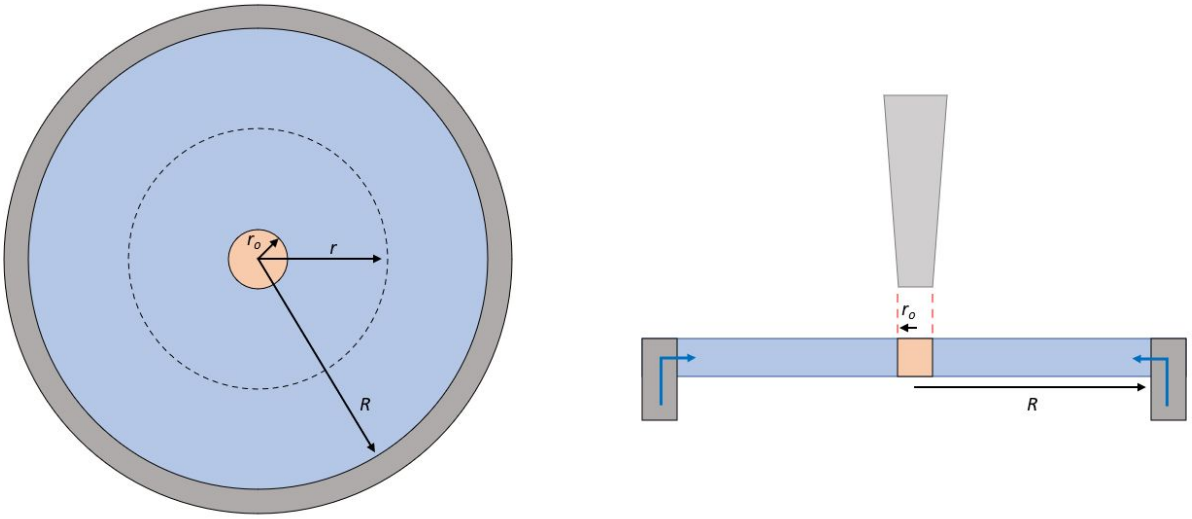

Fig. 1 Schematic for the inward, radial replenishment of fluid and evaporation by ambient and airflow induced methods.

Previous mathematical models have been developed which examine how physical and geometric variables factor into wicking behavior when evaporation is considered[36–38]. We define a similar system as developed by Conrath et al.[39] and Liu et al.[38] where a circular slice of porous media makes peripheral contact with an unlimited reservoir of fluid. At the perimeter of the porous slice, the capillary force induces the inward, radial penetration of liquid towards its center. At the center, a nozzle is positioned above the porous slice and generates a flow of air that is constrained within the nozzle radius. To model the system as a two-dimensional problem using planar coordinates, we assume that the thickness of the slice is much smaller than the radial dimensions.

During the enrichment process, two methods of evaporation occur on the wetted surface of the porous slice. The first is the ambient evaporation that is not affected by airflow, and the second is the airflow-induced evaporation. We therefore consider the total evaporation rate, K, which is the volume of evaporated liquid per area and time (*cm³/m²·s*) and is the sum of the ambient evaporation (K_o) and the airflow-induced evaporation (K_1):

$$K(r) = K_o + K_1 u(r_o - r) \qquad (1)$$

where r_o is the radius of the airflow jet and *u* represents a unit step function. Here, we assume that all evaporation will only occur on the top surface of the filter and that the airflow speed above the filter surface is negligible outside r_o.

When the steady state is reached and the enriched area under the nozzle has not completely dried, the continuity equation can be written as

$$2\pi r K(r) = -\frac{dF(r)}{dr} \quad (2)$$

where *F* refers to the volumetric flux of water per time (*cm³/s*)

In order to drive the flux, Darcy's law for liquid flow can be expressed as:

$$\frac{F}{A} = -\frac{S dP}{\eta dr} \quad (3)$$

where the flux, *F*, of liquid flow is through a cylindrical surface having area $A = 2\pi r h\gamma$, S is the permeability of the porous medium, γ is the porosity of the membrane, η is the liquid viscosity, and P is the pressure of the liquid. Substituting the cylindrical area into equation 3 and solving for the volumetric flux yields,

$$F = -\frac{2\pi h\gamma S}{\eta} r \frac{dP}{dr} \quad (4)$$

Substituting eq (4) into eq (2) and combining with eq (1), we obtain

$$[K_o + K_1 u(r_o - r)] = \frac{h\gamma S}{\eta}\left[\frac{d^2P}{dr^2} + \frac{1 dP}{r\, dr}\right] \quad (5)$$

We define the boundary conditions as:

$$P(R) = P_c, \ \frac{dP}{dr}|_{r=0} = 0 \ \ (see\ Supplmentary\ for\ this\ BC)$$

where P_c is the capillary pressure having the form:

$$P_c = \frac{2\sigma\ cos\theta_S}{R_{eff}} \qquad (6)$$

where σ is the surface tension, θ_s is the contact angle formed between solid and liquid, and R_{eff} is the effective pore radius of the porous medium.

$$P(r) = \frac{-\eta}{4h\gamma S}(K_o)(R^2 - r_o^2) - \frac{\eta}{4h\gamma S}(K_o + K_1)(r_o^2 - r^2) + P_c \qquad 0 \leq r \leq r_o$$

$$P(r) = \frac{-\eta}{4h\gamma S}(K_o)(R^2 - r^2) + P_c \qquad R \geq r \geq r_o \qquad (7)$$

$$P(r) \geq 0 \ \ for\ all\ r. \quad When\ P(r) = 0\ at\ a\ certain\ r,\ the\ region\ is\ dried\ up.$$

$$F(r_o) = -\frac{2\pi h\gamma S}{\eta} r\frac{dP}{dr}|_{r_o} = \pi {r_0}^2(K_o + K_1) \qquad (8)$$

We assume that when the wetted porous slice undergoes evaporation, it experiences varying degrees of water saturation. We therefore use the relation:

$$P(r) = P_c n(r) \qquad 0 \leq n(r) \leq 1 \ \ (9)$$

where n is the fraction of the pores (capillaries) that are completely saturated with water.

Integrating to find the water volume within r_o, the region under the air flow,

$$V(r_o) = 2\pi h\gamma \int_0^{r_o} n(r) r dr = \pi h\gamma r_o^2 - \frac{\pi\eta r_o^2}{8P_c S}\left[K_o(2R^2 - r_o^2) + K_1 r_o^2\right] \qquad (10)$$

The ratio between the volume from the water flux and the volume under the air flow determines the enrichment factor, a value which characterizes how effectively solutes are transported and concentrated under the airflow spot:

$$EF\ (enrichment\ factor) = \frac{F(r_o)t}{V(r_o)} = \frac{(K_o + K_1)t}{h\gamma + \frac{\eta}{8P_cS}\left[K_1 r_o^2 - K_o(2R^2 - r_o^2)\right]} \qquad (11)$$

As the enrichment method utilizes a rapid jet of low humidity air to promote evaporation, we have operated under the condition $K_1 r_o^2 \gg K_o R^2$ in all cases regardless of environmental humidity and temperature. This condition can be readily achieved because wetted, porous materials develop a saturated boundary layer which can be more easily displaced with airflow. Under this condition, (11) becomes

$$EF\ (enrichment\ factor) = \frac{F(r_o)t}{V(r_o)} \sim \frac{K_1}{h\gamma + \frac{\eta}{8P_cS}K_1 r_o^2}t \qquad (12)$$

Therefore, within a given time period, the variables governed by the airflow (K_1, r_o) can be controlled to maximize the enrichment factor. The influence of these variables according to Eq. (11) is shown in **Fig 2.**, where the enrichment factor is plotted as a function of r_o for different K_1 using tabulated values for the physical (S, η, P_c, γ, etc.) parameters [40,41]. Because the evaporation rate for a saturated, porous material behaves like that of a free surface of water [42], the ambient evaporation rate was set as 0.1uL/min for a circular slice of material with R = 0.5cm[43]. While r_o is a simple geometric parameter, K_1 is influenced by a

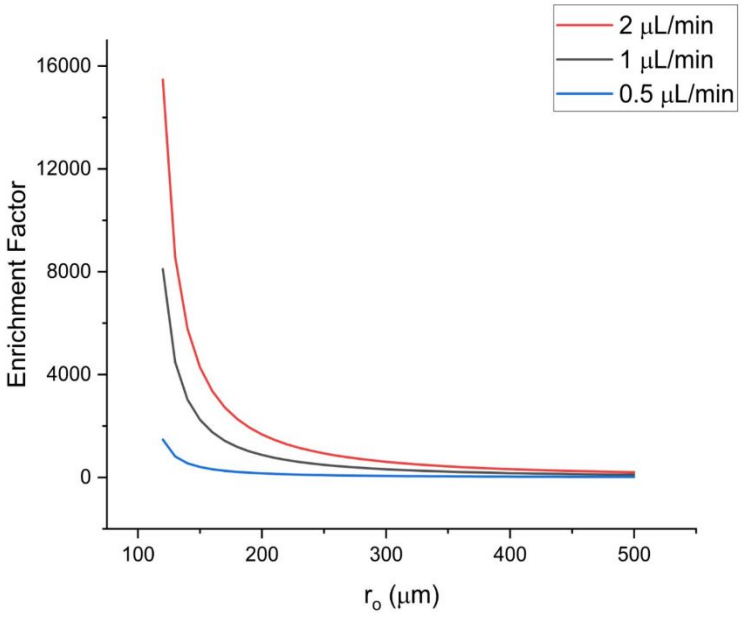

Figure 2. Enrichment Factor v. airjet radius for different evaporation rates after 10 minutes of enrichment

variety of factors including airflow speed, air flow temperature etc. These factors were incorporated into K_1 to simplify the model, however present additional degrees of freedom when looking to further increase the enrichment factor.

2.2 Overview of airflow-based enrichment on paper

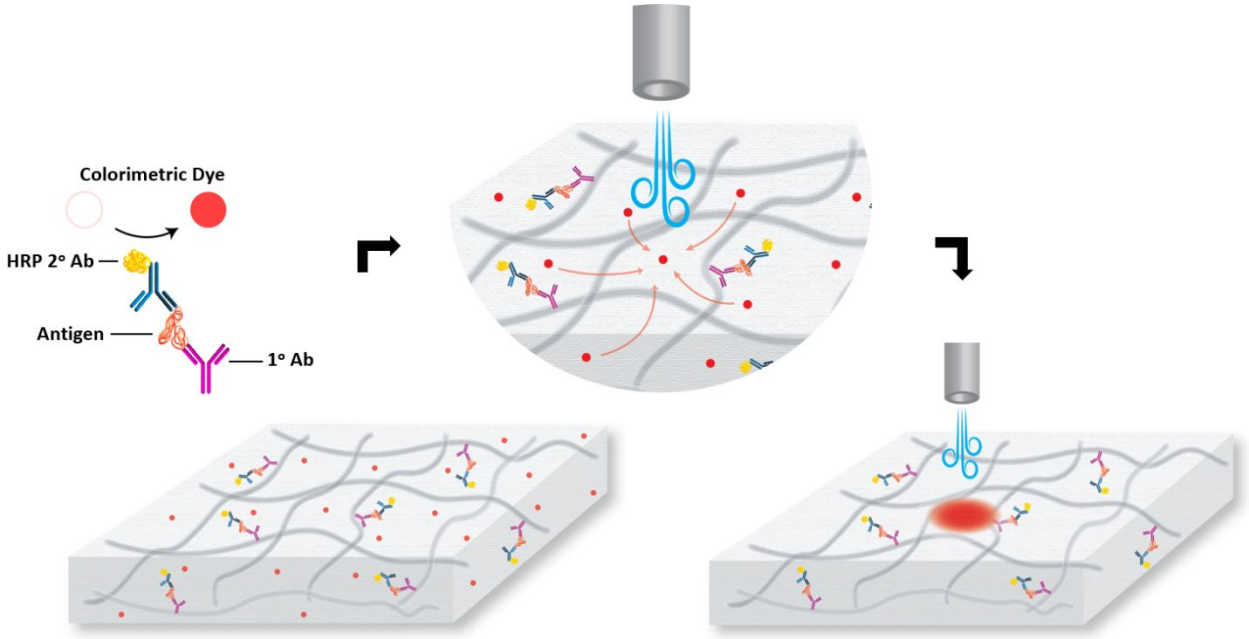

Figure 3. Schematic of the airflow-based enrichment for the concentration of colorimetric substrates produced during on-paper ELISA.

Fig. 3 depicts the operation principle for airflow-based enrichment in a paper matrix, using ELISA as an example for the purpose of illustration. This technique occurs on a pre-wetted filter. A nozzle connected to a nitrogen source is brought down perpendicular to the filter, and nitrogen is blown to create an evaporative gradient by reducing the thickness of a boundary layer containing saturated water vapor immediately above the surface[44,45]. While any compressed air source can accomplish this, nitrogen was chosen as it is a "dry" (low humidity) source of airflow and gave consistent enrichment results when compared to compressed, ambient air. Due to accelerated localized evaporation by the nitrogen airflow, fluid flows driven by capillary action will converge towards the area under the jet air from the filter's periphery to replenish the lost water. In doing so, any dissolved solutes will be carried by the flow and eventually accumulate underneath the nozzle. The enrichment factor derived previously is therefore a measurement of how concentrated the solutes become and how small the accumulation spot is. We aim to use this technique to enhance the visibility and sensitivity of nucleic acid and protein colorimetric detection assays – including ELISA. For these assays, the colorimetric substance can be enriched to a single spot under the nozzle to improve the uniformity and concentration in addition to easier detection.

2.3 Static or dynamic movement of the airflow nozzle leads to solute enrichment and movement

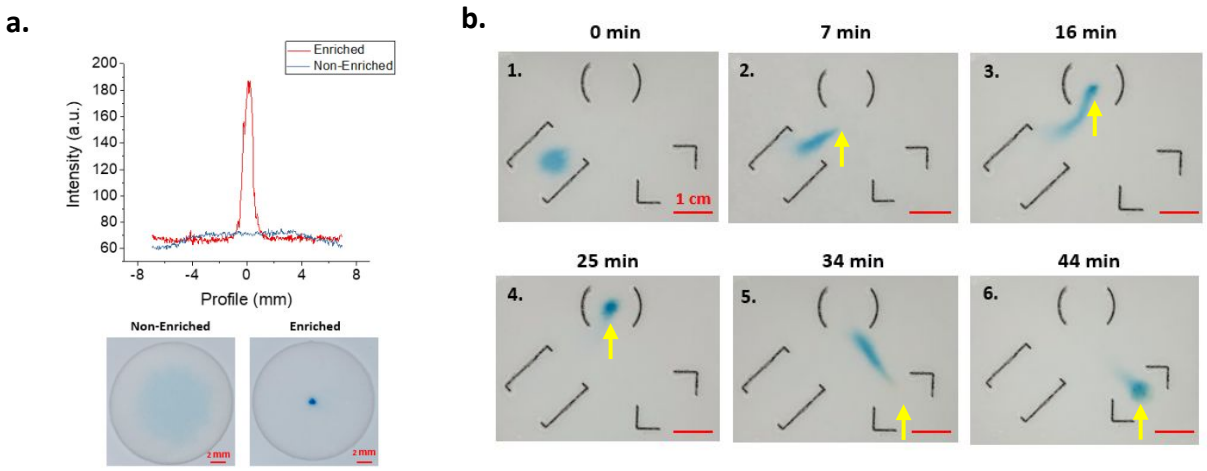

Figure 4. **(a.)** Profile plot of pixel intensity for enriched and non-enriched samples of dye deposited on paper. Images underneath represent corresponding non-enriched (before) and enriched (after) sample. **(b.)** Image sequence of dye localization in paper with hydrophobically patterned barriers indicated by black outlines. Images were taken during specified time points during dynamic movement of the nozzle. Actual nozzle position is indicated by the yellow arrow.

Airflow enrichment can accommodate two modes of fluid movement depending on whether the nozzle is in a static or dynamic position. When the nozzle position remains fixed **(Fig 4a.)**, solute enrichment occurs as evaporative-loss leads to capillary-induced replenishment from the surrounding area. To visualize this effect, 7 uL of a blue, diluted dye solution was deposited on a 16mm diameter filter cutout. The cutout was placed concentric to a replenishing pad saturated with water, and a 200um diameter nozzle was aimed perpendicular to the surface. Initiating the airflow establishes an evaporative gradient which generates fluid flows that are directed radially inward and transports the dye from a larger area to a defined spot. In addition to these flows along the 2D plane, any solutes will also move and localize at the paper's surface due to evaporation being a surface-driven phenomenon. As seen in the profile plot, this three-dimensional transport can thereby enhance visualization and detection of the initially diluted dye as it becomes more uniformly concentrated and unobscured from interacting with light.

Dynamic movement of the nozzle allows transportation of the solute to specified positions along the paper surface. The transport mechanism remains the same as the enrichment process, but the continual re-establishment of new evaporative gradients allows the direction of the replenishing flows to be controlled. In **Fig 4b.**, 1uL of blue dye was deposited on a wetted filter paper with hydrophobic patterns. The patterned filter paper was placed concentric to a replenishing pad saturated with water to prevent the paper from drying out. As less emphasis is placed on the degree of enrichment and more on the speed of transport, a wider 1.5 mm (should it be 1.5mm? 1.5cm seems to be huge) diameter nozzle accompanied with higher airflow speeds were used in comparison to that of the static enrichment. As shown in **Fig 4b.**, the localization of the dye can be controlled simply by changing the position of the nozzle above the paper surface.

2.4 Sequential delivery using the airflow-enrichment method

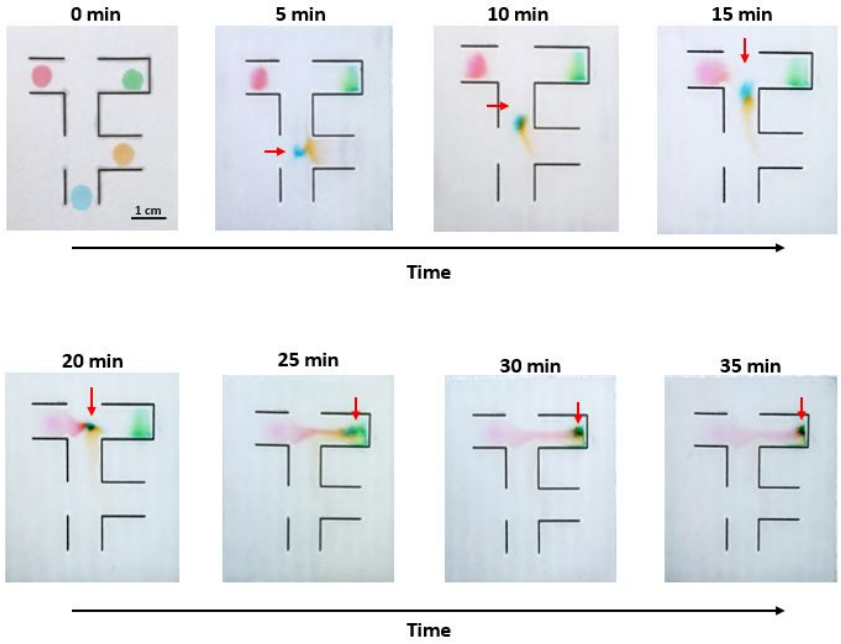

Figure 5. Image sequence for the sequential delivery of colored dyes by moving the airflow spot (red arrow) on a paper device patterned with PDMS channels. Black outlines represent the hydrophobic barriers and breaks in the outline indicate inlets to the channel design.

We demonstrate how controlled delivery of multiple reagents, visualized by different dye colors, can be accomplished using the airflow enrichment technique **(Fig. 5)**. On a piece of filter paper patterned with hydrophobic channels, a combination of static and dynamic nozzle movements serves to mix and transport specified reagents, respectively. The filter paper is overlayed concentric to a replenishing pad cutout, such that contact between the two materials was only made at the paper's perimeter. Then, 1uL of each dye color was spotted on the paper and could be mixed in a stepwise fashion based on the position of the nozzle - indicated by the red arrow. For this setup, water is transferred from the replenishing pad to the filter paper and eventually moves towards the interior of the channel through the openings in the design. While the openings act as inlets, the movement of the nozzle governs the position of the outlet and determines where fluid flows will converge. As there is only one nozzle (outlet) in this system, additional openings were incorporated to reduce backflow and prevent early mixing of downstream reagents. For sections where the dye was to remain stationary throughout the process, such as the green dye, a closed channel was created by walling off three sides to create an area of dead volume.

The advantage of airflow-enrichment lies in the mechanism responsible for fluid control. For many designs focused on sequential delivery, the primary driving force for fluid transport is through capillary action[4,46]. While capillarity is still present during airflow enrichment, it plays a secondary role with evaporation being the main driver of fluid movement. This has considerable effects when determining the overall design and costs of the assay. For one, conventional assays that rely on capillarity require relatively large sample volumes as they must continually imbue the device with the sample or running buffer in order to reach the detection zone[47,48]. For evaporative-driven transport, delivery of a small, initial volume of sample can

be dragged to downstream detection zones simply by guiding it with the nozzle. In this case, the nozzle was able to transport 1uL of the initial blue dye from beginning to end. In addition, for assays that require interactions between molecules to occur, the airflow technique allows for more efficient mixing. Rather than relying on the slower process of diffusion, the nozzle can be left in a static position such as in the 20- and 35-minute time points **(Fig. 5)** to facilitate the enrichment of different molecules and promote binding events. Finally, in designs that transport fluid through capillary action, the fluid flow is always "on" and specific obstructions are implemented in order to slow and control the flow rate for sequential delivery[23,46,47]. For evaporative driven transport, the fluid flow can be turned "on" and "off" depending on whether any air is being blown on the paper surface. The lack of any obstructions keeps the fabrication process simple and reduces the amount of space needed to accommodate the obstruction itself.

2.5 Application in a multistep Immunoassay

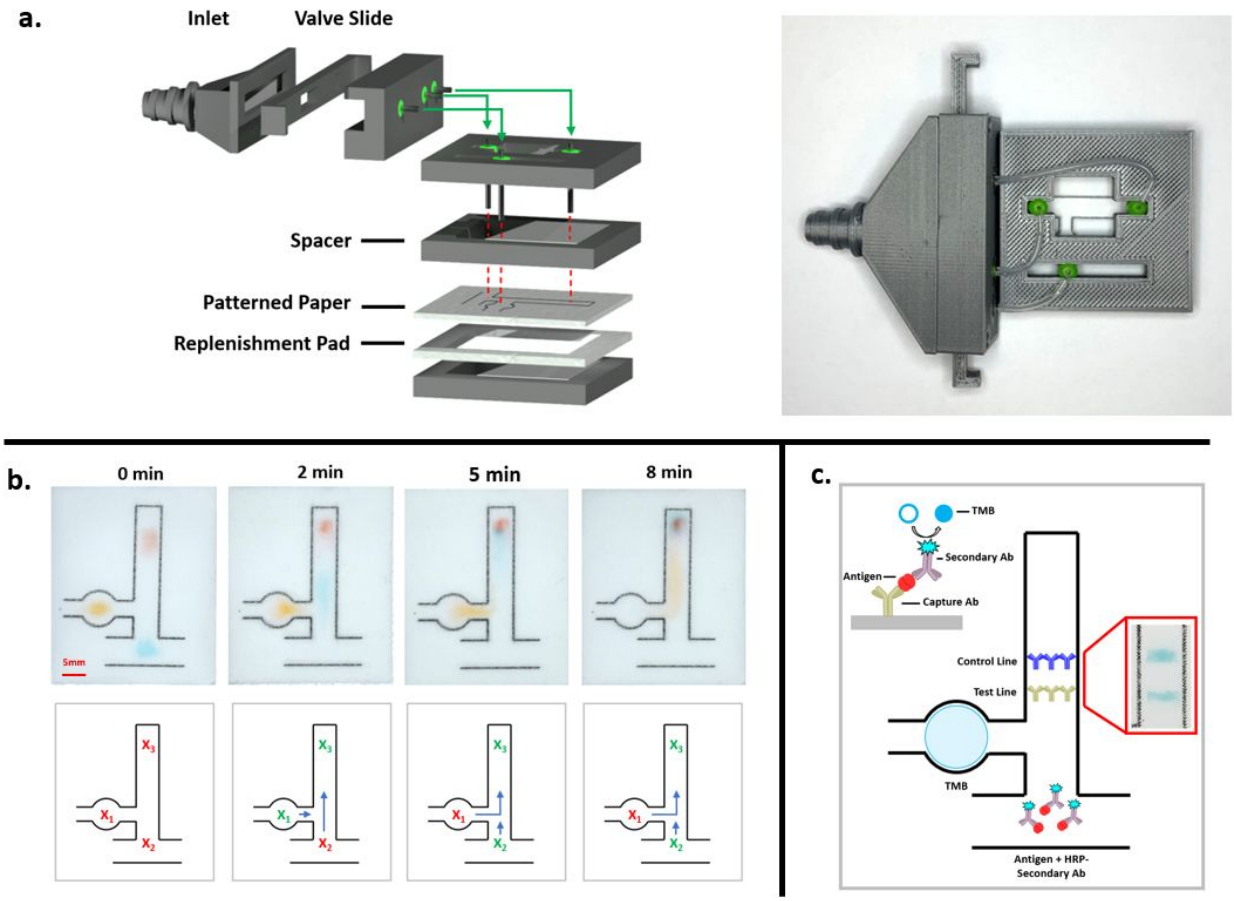

Figure 6. (a.) 3D-schematic of the POC device used for sequential delivery with the green arrows indicating tubing connections (left) and a top-down, real photo (right) of the assembled components. **(b.)** Demonstration of sequential delivery using dye as indicators. The top row shows the real photos taken at specified time points while the bottom row represents which nozzles are active (green) and inactive (red) as well as the strength of fluid flow from each channel (blue arrow). **(c.)** Schematic mapping the initial reagent spots for the multistep immunoassay. Red box is the real image of the test lines taken 32 minutes after starting the assay.

We next incorporate the airflow enrichment method in a possible POC device. In the previous figures, control of the fluid flow was dictated by the movement of a single nozzle and its relative position over the paper. As integrating a moving nozzle would be difficult in a POC device, we instead use a static arrangement of three individual nozzles (**Fig. 6a**) to accomplish step-wise delivery for an immunoassay. In addition, multiple nozzles were required as the dimensions of the patterned paper were reduced when compared in **Fig 3.** to decrease transport distances and consequently, the time for assay completion. Because of the constrained dimensions, a single nozzle cannot facilitate step-wise delivery as the evaporation would cause replenishing flows from multiple channels in the general vicinity. Therefore, for this setup, a single source of airflow originates from a central inlet and is then split up into the three separated nozzles - each of which the airflow can be turned on or off. The combination of active and inactive nozzles determines the predominant fluid flow within the patterned paper and therefore which reagent will be delivered faster (**Fig. S3**).

A demonstration of stepwise delivery as visualized with dye is shown (**Fig. 6b**), where the delivery of the blue dye is achieved prior to that of the orange dye through a combination of active nozzles. Within this system, we define two means of fluid transport – one is the evaporative mass transport caused by the airflow nozzles, and the other is the replenishment transport driven by capillarity in maintaining a constant level of water saturation in the entire membrane. For an active nozzle far from the replenishment pad and walled off such as pos. 3, the fluid has reached the terminal position and will simply evaporate off and deposit any solutes in this location. However, for activated nozzles closer to the replenishment pad such as pos. 1 and 2., the evaporation will reduce the amount of fluid entering the channel and thereby slow the net movement of the fluid. This in turn will cause the delay of fluid to enter the main channel and allow sequential delivery of reagents. Therefore, in **Fig 6b.**, the nozzles at X_1 and X_3 were first activated to delay movement of the orange dye such that the main replenishing flow was supplied by the blue channel. Once the blue dye reached the end, X_2 and X_3 were activated to allow the main source of replenishing flow from the orange dye.

The operation principle was then extended to an actual immunoassay, where 2uL of TMB, as well as 0.5uL of a pre-mixed solution of the antigen and the HRP-conjugated secondary antibody were deposited in separate channels (**Fig 6c**). Test and control lines were immobilized downstream of these reagents prior to running in PBST buffer. During the assay, the antigen-secondary antibody complex was first drawn up the channel by activating nozzles 1,3 for 10 minutes. Not only does this step first transport the antigen complex to the detection lines, but also acts as a washing step for the latter duration to remove any unbound proteins in this area. Then, the nozzles at pos. 2,3 were activated to begin moving the TMB to the detection lines. Once a faint signal could be seen in the control line, the airflow was stopped, and time was given to allow further color development. The signal from these lines were clearly visible using 4nM of the antigen after running the airflow for roughly 25 minutes and allowing an additional 5 minutes for color development. Comparing the time scales for this immunoassay with the dye demonstration in **Fig. 6b**, the immunoassay takes much longer to complete. We believe the longer duration is primarily caused by two factors: (i) the relative low solubility of the unreacted TMB which leads to a higher retention factor on paper and requires more fluid to be evaporated to move it through the channel, (ii) the high salt concentration in the PBST running buffer which, after prolonged evaporation, will crystallize in the paper and act as a barrier for further fluid migration. Additional time is therefore spent re-dissolving these barriers when the activated nozzles switch position.

2.6 Improving visualization on paper for colorimetric RT-LAMP

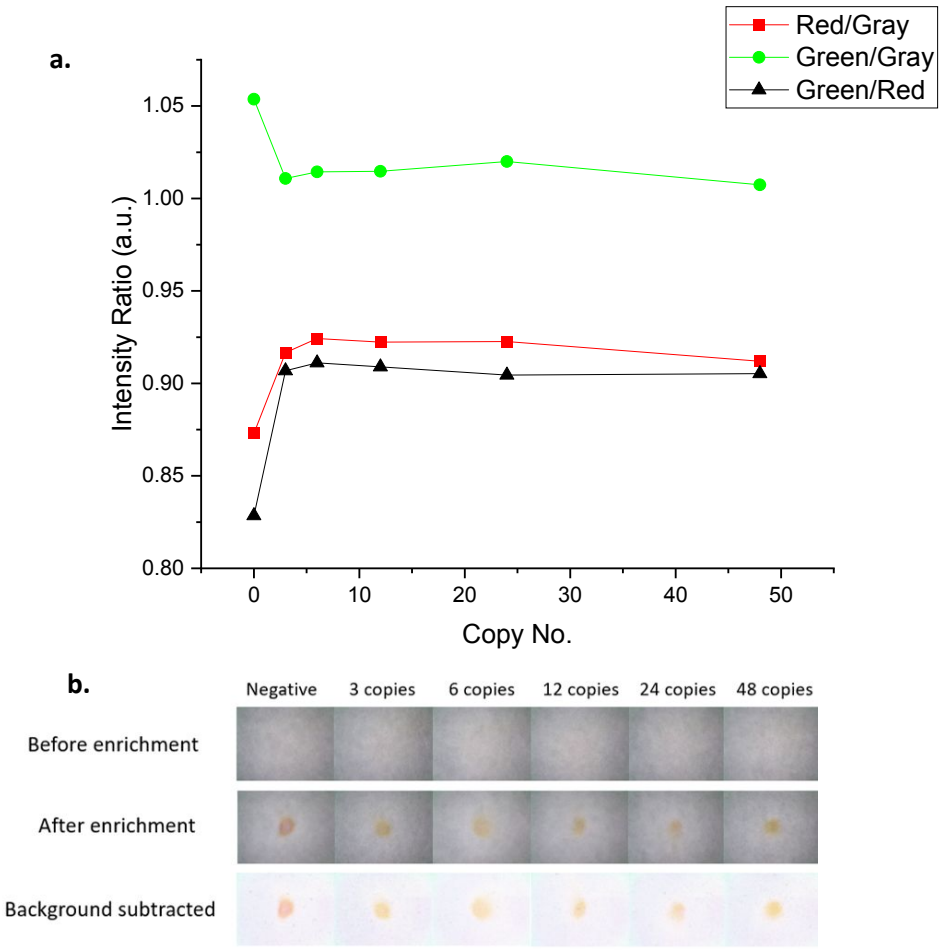

Figure 7. (a.) Plot of intensity ratio v. copy number between red and grayscale, green and grayscale, and green and red pixels. **(b.)** Before and after enrichment photos corresponding to different initial RNA copy numbers of the COVID-19 genome. Includes bottom "background subtracted" row to better visualize the color of each spot.

To test whether the airflow enrichment could improve visualization in already established colorimetric assays, the technique was incorporated for on paper RT-LAMP in the detection of the COVID-19 genome (**Fig. 7**). Heat inactivated viral particles were spiked in nuclease-free water to the desired concentrations and then amplified using a commercially available RT-LAMP kit. For all copy numbers, amplification via LAMP was performed in test tubes for 60 minutes prior to depositing 3uL of the LAMP product onto paper strips. The strips were connected to a replenishing flow of nuclease-free water, and the airflow was turned on for 5 minutes before imaging. As shown in **Fig. 7b**, comparison between the "before" and "after" enrichment demonstrates how the process drastically improves the visibility of the dye. Furthermore, the enrichment did not alter the results of the test. The pH-sensitive color of the RT-LAMP result, either red (negative) or yellow (positive), is influenced by polymerase activity which releases a proton per each incorporated nucleotide. As the enrichment involves the concentration of molecules, we may expect false positives to occur due to co-enrichment of hydronium ions. However, a large shift in the green/red pixel

intensity ratio from 0 (negative control) to 3 RNA copies supports the validity of the results as the negative control remains red.

Due to the presence of buffer in the master mix solution, the final enrichment spot remains larger than previously demonstrated in **Fig. 4a** as early salt crystallization inhibits further condensation. While additives can be considered to reduce salt build up, we chose not to include any as it may affect the pH of the solution and therefore the accuracy of the test. Even with a larger spot size, the results of the tests were still clear to the naked eye. The ease of integrating the airflow-based enrichment to various colorimetric assays, coupled with its short process time, demonstrates the flexibility and simplicity of the technique.

2.7 Improving on-paper ELISA sensitivity

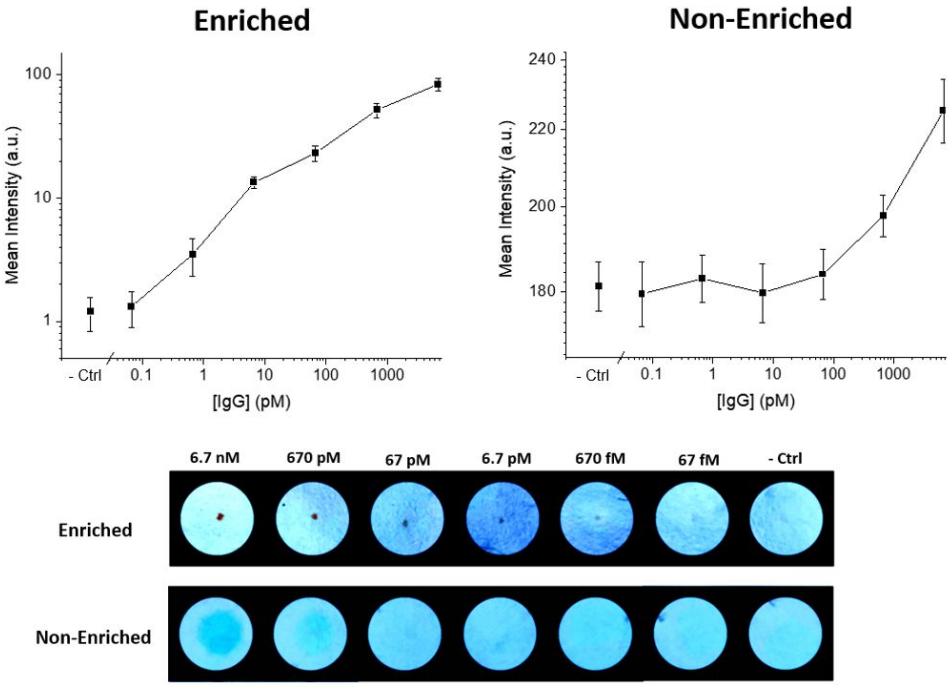

Figure 8: **(a.)** Comparison of Non-enriched and Enriched intensity plots for IgG concentrations from 67fM to 6.7nM. Error bars were calculated from three sets of experiments. **(b.)** Respective images from enriched and non-enriched samples from a single experimental set. Brightness and contrast were adjusted for better visualization of the TMB product.

We next use ELISA to model our enrichment method in improving the sensitivity for protein detection assays (**Fig. 8**). While ELISA on paper has attracted multiple studies in the past, a key obstacle in detection is due to the non-uniformity and unequal distribution of the colored substrate[4,13]. Therefore, achieving a high enrichment factor and being capable of transporting the substrate to a defined spot may increase the limit of detection. For this assay, TMB was chosen as the colorimetric substate as it has been shown to elicit one of the most sensitive responses in comparison with others. However, a drawback of using TMB lies in the relative insolubility of the oxidized product in water which hinders the formation of an airflow-enriched spot. Therefore, the addition of the 0.1% glycerol (v/v) in 2M HCl “stop” solution served

multiple purposes. The first was to prevent further development of the substrate during enrichment and keep the colorimetric development times consistent between the enriched and non-enriched samples. The second was to protonate the TMB product to increase its solubility for enrichment. Glycerol was also added in small amounts to prevent early salt crystallization which halts spot formation during the evaporative process. The addition of an acidic solution to the TMB product causes a color change from blue to yellow which explains the different colors between the enriched and non-enriched samples. Despite the color change, the enriched samples were able to distinguish antigen concentrations by more than 2 orders of magnitude as compared to the non-enriched samples while only spending 15 minutes under airflow. This demonstrates the ease at which airflow enrichment can be integrated in current detection-based assays given the fraction of time needed to conduct the process and the much-improved detection sensitivity.

3. Materials and Methods

3.1 Colorimetric Assay Reagents

For the RT-LAMP assay, WarmStart Colorimetric RT-LAMP 2X Master Mix (DNA and RNA) were purchased from New England Biolabs. The RT-LAMP primers against Nucleocapsid (N-1) and ORFla-1 genes were synthesized by Integrated DNA Technologies (IDT) and were designed according to a similar assay[49].The SARS-CoV-2 RNA (VR-3280SD) was purchased from American Type Culture Collection (ATCC) with an initial copy number of $3.4x10^5$ genome copies/ µL. For ELISA, Rabbit IgG, goat anti-rabbit IgG, TMB, mouse anti-goat IgG, Ultrapure water, 25% glutaraldehyde and chitosan were purchased from Millipore Sigma. Anti-rabbit IgG antibody conjugated with HRP was purchased from VectorLabs. The blocking buffer was comprised of 0.05% v/v Tween-20 and 1% w/v bovine serum albumin (BSA) in 1X phosphate-buffered saline (PBS). The antibody incubation solution consisted of the blocking buffer with the conjugated antibody at a 1:4000 ratio.

3.2 Enrichment Setup

Pre-pulled, 1mm O.D. capillaries were purchased from Tritech Research and the tips were sanded down to roughly 200um in diameter. A single tip was mounted on an xyz-stage through a 3D-printed holder and connected to a nitrogen source by rubber tubing. The mass flow rate was adjusted by pressure valves incorporated along the rubber tubing and specific values were determined by a mass flow meter purchased from Sierra Instruments. The specified sample was deposited on a cutout of Watman No. 1 filter paper and placed on a hollowed-out replenishing pad comprised of blotting paper saturated with water. The contact between the filter cutout and the replenishing pad only occurred at the perimeter of the filter cutout (Fig. S1). This arrangement was then placed on a 3D-printed platform that also contained a hollow section and the capillary tip was brought about 2mm above the filter piece.

3.3 Enrichment of dye

The filter paper was punched into circular, 16 mm diameter cutouts and initially wetted with 10uL of DI water. After allowing the water to spread, 3uL of a diluted food dye solution was added to the center of the cutout which was then overlayed on top of a hollowed-replenishing pad saturated with DI water. The section was placed under the capillary tip and the nitrogen flow was turned on to a rate of 0.1 l/min.

Airflow enrichment occurred for 15 minutes before imaging the section under a desktop ring-light using an iPhone 10 camera.

3.4 Fluid control

Patterns and outlines were designed using CAD software and printed directly on filter paper. The outlines were then traced over using a syringe containing a 10:1 ratio of PDMS to curing agent and subsequently placed in a 60°C oven to cure for 1 hour. Prior to enrichment, the patterned filter paper was dampened with DI water and 1uL of dye was spotted in the starting positions. The patterned filter paper was then placed on a water-saturated replenishing pad and positioned 2mm under a 1.5 cm diameter metal nozzle with a nitrogen flow of 0.25 l/min. The relative position of the nozzle was changed by moving the platform with the filter paper.

3.5 Application into Multistep Immunoassay

The 3D models for the POC device were designed using 3D CAD software and printed. Rubber gaskets were placed in the openings and glass capillaries (1mm O.D./0.7mm I.D.) were inserted in the specified areas and connected with rubber tubing. The patterned paper and dye demonstration was performed in the same manner to **3.4**. For the immunoassay, the channels were treated with 0.25mg/mg chitosan (in 1% acetic acid) and allowed to dry completely before adding 2.5% glutaraldehyde and incubating for 1 hour. The treated paper was then washed in a wash bath containing 1X PBS and allowed to dry before striping the test and control lines comprised of 0.2mg/mL of goat anti-rabbit antibody and 0.39mg/mL of mouse anti-goat antibody, respectively. The paper was then blocked for 30 minutes and subsequently allowed to dry in a desiccator. Before performing the assay, 0.5uL of solution containing 1:2000 reporter antibody and 4nM rabbit IgG was deposited in one channel, and 2uL of TMB was deposited in the other. The paper was then pre-wetted by pressing it against a saturated membrane containing PBST, before placing it on another hollowed replenishment pad also containing PBST. The pads were placed in the POCT device and the airflow was started. Images of the paper were taken with an iPhone 10 camera under a ring LED light.

3.6 Enrichment of RT-LAMP products on paper

Colorimetric LAMP was performed by adding 1 µL of the specified copy number of isolated SARS-CoV-2 RNA, 12.5 µL of the WarmStart Colorimetric RT-LAMP 2x Master Mix, 2.5 µL of the 10x primer mix and diluting with nuclease free water up to 25uL in total volume. All the solutions were prepared fresh and kept in closed test tubes to limit exposure to atmospheric CO_2. The reactions were then incubated in a 65 °C oven for 60 min. The RT-LAMP samples were then taken out and placed on ice for 30 seconds before being stored at room temperature. For the enrichment, filter paper was cut into strips and 3uL each RT-LAMP product was deposited in the middle. Enrichment was carried out for 5 minutes with at 5uL/min replenishing flow of nuclease-free water from syringe pumps purchased from Harvard Apparatus. Before and after images were taken by a digital microscopic camera (AM7115MZT, Dino-Lite) with preset image capture settings.

3.7 RT-LAMP colorimetric readout signal analysis

The image signal analysis process of RT-LAMP colorimetric readout is shown in Figure S3. The effect of the GAMMA correction on the captured image is eliminated on the original image to remove the biased on the pixel intensity introduced by GAMMA correction [2]. The original image is subtracted by the background level first to remove the noise introduced from the background. A binary mask is generated through fixed intensity thresholding and preset enrichment spot size to determine the region of interest (ROI). The processed image is then convoluted with the binary mask to exclude pixels outside of the ROI. The convoluted color image is split into single color channels, and the average pixel intensity is calculated based on the average pixel intensity of the RGB color channel images. The image processing pipeline is developed based on ImageJ and MATLAB. All enrichment sample paper is processed using the same pipeline and parameter setting.

3.8 On-Paper ELISA

Double-sided tape was placed on a 3D-printed plate containing a 3 x 3 array of 12mm diameter holes (Fig. S5). The tape was cut out around the holes and 16mm diameter filter circles were overlayed on top with only the perimeter making contact. Enhanced antibody immobilization was performed by adding 20uL of 0.25mg/mg chitosan (in 1% acetic acid) to all filter circles and letting them dry completely[50–52]. Then 20uL of 2.5% glutaraldehyde in 1X PBS was added to the circles and the plate was covered with a petri dish for 1 hour to avoid evaporation. Each circle was then washed four times with 20uL of PBS with the excess liquid being removed between washes by pressing the plate against blotting paper. After washing, 10uL of the capture antibody solution was deposited and allowed to incubate for 30 minutes. The circles were washed four times with 20uL of PBS and successively blocked with 30uL of blocking buffer for an additional 30 minutes. After blocking, the circles were washed once with 20uL of PBS and 3uL of the Rabbit IgG at specified concentrations was added to each circle. This was incubated for 15 minutes before adding 7 uL of the secondary antibody solution and incubating for another 2 minutes. The circles were then removed from the plate and into a wash bath containing 0.05% Tween in 1X PBS and a separator to prevent individual circles from contacting each other. The wash bath was placed on a shaker for 30 minutes with the wash solution being changed out every 10 minutes. The circles were then stored in 1X PBS until use.

3.8 Comparison between Enriched and Non-enriched Samples

For the non-enriched sample, the circles were removed from the PBS and transferred on blotting paper to remove excess liquid prior to being placed on a cleaned plate. The color development was initiated by adding 7 uL of TMB solution and allowing 80 seconds for the reaction to proceed before imaging under a desktop ring-light. A similar procedure was performed with the enriched samples except that the reaction time was shortened to 70 seconds to include a washing step afterwards. This step consisted of transferring the circle onto blotting paper and depositing 1 mL of ultrapure water to reduce salt levels. Then, 6 uL of 0.1% glycerol (v/v) in 2M HCl was added to the circle to stop the reaction during the enrichment process. The circle was enriched under the 200um diameter capillary nozzle for 15 minutes until completely dry and imaged under the ring-light.

3.9 ELISA Imaging

The images were processed through ImageJ by first subtracting the background by 50 pixels, then enhancing the contrast (Analyze → Enhance Contrast) by 0.3%.The images were then split into RGB color

channels and inverted. For the non-enriched samples, the selected ROI consisted of the entire filter circle diameter. In the enriched samples, a binary mask was used to highlight the enriched area and the ROI consisted of a 2mm diameter section around the highlight. After finding the mean respective mean intensities from each channel, the magnitude of the combined channels was calculated for the mean intensity.

4. Conclusion

To summarize, we present a simple, airflow-based method that can manipulate fluid flows in paper matrices. Depending on how the method is used, enrichment or lateral transportation of solutes can be performed using minimal external equipment. The enrichment process was integrated into existing colorimetric assays for genomic and proteomic detection to significantly enhance the visualization and sensitivity of the assays. While the enrichment aspect was explored in depth for this study, we also demonstrate how multistep, sequential delivery of reagents can be accomplished for future assays requiring higher complexity. This method ultimately presents a unique example where sensitivity improvement and fluid control can be accomplished using a single technique. Despite focusing on colorimetric detection assays in this study, we envision that this method can be easily incorporated into the broader field of mPADs.

5. Conflicts of Interest

There are no conflicts of interests to declare.

6. Acknowledgements

This research is based upon work supported in part by the Office of the Director of National Intelligence (ODNI), Intelligence Advanced Research Projects Activity (IARPA), via 2020-20090400002. The views and conclusions contained herein are those of the authors and should not be interpreted as necessarily representing the official policies, either expressed or implied, of ODNI, IARPA, or the U.S. Government. The U.S. Government is authorized to reproduce and distribute reprints for governmental purposes notwithstanding any copyright annotation therein. This work was performed, in part, at the San Diego Nanotechnology Infrastructure (SDNI) of UCSD, a member of the National Nanotechnology Coordinated Infrastructure (NNCI), which is supported by the National Science Foundation (Grant No. ECCS-1542148).

7. References:

1. Lisowski P, Zarzycki PK. Microfluidic paper-based analytical devices (μPADs) and micro total analysis systems (μTAS): Development, applications and future trends [Internet]. Chromatographia2013 [cited 2021 May 26];76(19–20):1201–14. Available from: http://www.wbiis.tu.koszalin.pl/labtox

2. Whitesides GM. The origins and the future of microfluidics. Nature2006;442(7101):368–73.

3. Yetisen AK, Akram MS, Lowe CR. Paper-based microfluidic point-of-care diagnostic devices [Internet]. Lab on a Chip2013 [cited 2021 May 26];13(12):2210–51. Available from: www.rsc.org/loc

4. Akyazi T, Basabe-Desmonts L, Benito-Lopez F. Review on microfluidic paper-based analytical devices towards commercialisation. Analytica Chimica Acta2018;1001:1–17.

5. Nery EW, Kubota LT. Sensing approaches on paper-based devices: A review. Analytical and Bioanalytical Chemistry2013;405(24):7573–95.

6. Abe K, Suzuki K, Citterio D. Inkjet-printed microfluidic multianalyte chemical sensing paper. Analytical Chemistry [Internet] 2008 [cited 2021 May 28];80(18):6928–34. Available from: https://pubs.acs.org/sharingguidelines

7. Martinez AW, Phillips ST, Butte MJ, Whitesides GM. Patterned paper as a platform for inexpensive, low-volume, portable bioassays. Angewandte Chemie - International Edition [Internet] 2007 [cited 2021 May 28];46(8):1318–20. Available from: http://www.angewandte.orgorfromtheauthor.

8. Ornatska M, Sharpe E, Andreescu D, Andreescu S. Paper bioassay based on ceria nanoparticles as colorimetric probes. Analytical Chemistry 2011;83(11):4273–80.

9. Choleva TG, Kappi FA, Giokas DL, Vlessidis AG. Paper-based assay of antioxidant activity using analyte-mediated on-paper nucleation of gold nanoparticles as colorimetric probes. Analytica Chimica Acta 2015;860:61–9.

10. Teengam P, Siangproh W, Tuantranont A, Vilaivan T, Chailapakul O, Henry CS. Multiplex Paper-Based Colorimetric DNA Sensor Using Pyrrolidinyl Peptide Nucleic Acid-Induced AgNPs Aggregation for Detecting MERS-CoV, MTB, and HPV Oligonucleotides. Analytical Chemistry [Internet] 2017 [cited 2021 May 28];89(10):5428–35. Available from: https://pubs.acs.org/sharingguidelines

11. Chen W, Fang X, Li H, Cao H, Kong J. A Simple Paper-Based Colorimetric Device for Rapid Mercury(II) Assay. Scientific Reports [Internet] 2016 [cited 2021 May 28];6(1):1–7. Available from: www.nature.com/scientificreports

12. Wang X, Li F, Cai Z, Liu K, Li J, Zhang B, et al. Sensitive colorimetric assay for uric acid and glucose detection based on multilayer-modified paper with smartphone as signal readout. Analytical and Bioanalytical Chemistry [Internet] 2018 [cited 2021 May 28];410(10):2647–55. Available from: https://doi.org/10.1007/s00216-018-0939-4

13. Hu J, Wang SQ, Wang L, Li F, Pingguan-Murphy B, Lu TJ, et al. Advances in paper-based point-of-care diagnostics. Biosensors and Bioelectronics2014;54:585–97.

14. Parolo C, de la Escosura-Muñiz A, Merkoçi A. Enhanced lateral flow immunoassay using gold nanoparticles loaded with enzymes. Biosensors and Bioelectronics 2013;40(1):412–6.

15. Sakurai A, Takayama K, Nomura N, Yamamoto N, Sakoda Y, Kobayashi Y, et al. Multi-colored immunochromatography using nanobeads for rapid and sensitive typing of seasonal influenza viruses. Journal of Virological Methods 2014;209:62–8.

16. Yao L, Teng J, Zhu M, Zheng L, Zhong Y, Liu G, et al. MWCNTs based high sensitive lateral flow strip biosensor for rapid determination of aqueous mercury ions. Biosensors and Bioelectronics 2016;85:331–6.

17. Shirshahi V, Tabatabaei SN, Hatamie S, Saber R. Functionalized reduced graphene oxide as a lateral flow immuneassay label for one-step detection of Escherichia coli O157:H7. Journal of Pharmaceutical and Biomedical Analysis 2019;164:104–11.

18. Kim W, Lee S, Jeon S. Enhanced sensitivity of lateral flow immunoassays by using water-soluble nanofibers and silver-enhancement reactions. Sensors and Actuators, B: Chemical 2018;273:1323–7.

19. Rodríguez MO, Covián LB, García AC, Blanco-López MC. Silver and gold enhancement methods for lateral flow immunoassays. Talanta 2016;148:272–8.

20. Kasetsirikul S, Shiddiky MJA, Nguyen NT. Challenges and perspectives in the development of paper-based lateral flow assays [Internet]. Microfluidics and Nanofluidics2020 [cited 2021 May 28];24(2):17. Available from: https://doi.org/10.1007/s10404-020-2321-z

21. Kim TH, Hahn YK, Kim MS. Recent Advances of Fluid Manipulation Technologies in Microfluidic Paper-Based Analytical Devices (μPADs) toward Multi-Step Assays. Micromachines 2020, Vol 11, Page 269 [Internet] 2020 [cited 2021 Sep 16];11(3):269. Available from: https://www.mdpi.com/2072-666X/11/3/269/htm

22. Jahanshahi-Anbuhi S, Henry A, Leung V, Sicard C, Pennings K, Pelton R, et al. Paper-based microfluidics with an erodible polymeric bridge giving controlled release and timed flow shutoff. Lab on a Chip [Internet] 2014 [cited 2021 Jun 2];14(1):229–36. Available from: www.rsc.org/loc

23. Lutz B, Liang T, Fu E, Ramachandran S, Kauffman P, Yager P. Dissolvable fluidic time delays for programming multi-step assays in instrument-free paper diagnostics. Lab on a Chip [Internet] 2013 [cited 2021 May 31];13(14):2840–7. Available from: www.rsc.org/loc

24. Lafleur LK, Bishop JD, Heiniger EK, Gallagher RP, Wheeler MD, Kauffman P, et al. A rapid, instrument-free, sample-to-result nucleic acid amplification test. Lab on a Chip [Internet] 2016 [cited 2021 Jun 2];16(19):3777–87. Available from: www.rsc.org/loc

25. Koo CKW, He F, Nugen SR. An inkjet-printed electrowetting valve for paper-fluidic sensors. Analyst [Internet] 2013 [cited 2021 Jun 2];138(17):4998–5004. Available from: www.rsc.org/analyst

26. Li X, Tian J, Shen W. Progress in patterned paper sizing for fabrication of paper-based microfluidic sensors. Cellulose [Internet] 2010 [cited 2021 Jun 2];17(3):649–59. Available from: https://link.springer.com/article/10.1007/s10570-010-9401-2

27. Park J, Shin JH, Park J-K. Pressed Paper-Based Dipstick for Detection of Foodborne Pathogens with Multistep Reactions. 2016 [cited 2021 Sep 16];Available from: https://pubs.acs.org/sharingguidelines

28. Preechakasedkit P, Siangproh W, Khongchareonporn N, Ngamrojanavanich N, Chailapakul O. Development of an automated wax-printed paper-based lateral flow device for alpha-fetoprotein enzyme-linked immunosorbent assay. Biosensors and Bioelectronics 2018;102:27–32.

29. Fu E, Lutz B, Kauffman P, Yager P. Controlled reagent transport in disposable 2D paper networks. Lab on a Chip [Internet] 2010 [cited 2021 May 28];10(7):918–20. Available from: www.chembio.com/newtechnologies.html.

30. Kim TH, Hahn YK, Lee J, Noort D van, Kim MS. Solenoid Driven Pressure Valve System: Toward Versatile Fluidic Control in Paper Microfluidics. Analytical Chemistry [Internet] 2018 [cited 2021 Sep 18];90(4):2534–41. Available from: https://pubs.acs.org/doi/full/10.1021/acs.analchem.7b03791

31. J. Toley B, A. Wang J, Mayuri Gupta, R. Buser J, K. Lafleur L, R. Lutz B, et al. A versatile valving toolkit for automating fluidic operations in paper microfluidic devices. Lab on a Chip [Internet] 2015 [cited 2021 Sep 18];15(6):1432–44. Available from: https://pubs.rsc.org/en/content/articlehtml/2015/lc/c4lc01155d

32. Fratzl M, Chang BS, Oyola-Reynoso S, Blaire G, Delshadi S, Devillers T, et al. Magnetic Two-Way Valves for Paper-Based Capillary-Driven Microfluidic Devices. ACS Omega [Internet] 2018 [cited 2021 Sep 18];3(2):2049–57. Available from: https://pubs.acs.org/doi/full/10.1021/acsomega.7b01839

33. Verma MS, Tsaloglou MN, Sisley T, Christodouleas D, Chen A, Milette J, et al. Sliding-strip microfluidic device enables ELISA on paper. Biosensors and Bioelectronics 2018;99:77–84.

34. Ho Shin J, Park J-K. Functional Packaging of Lateral Flow Strip Allows Simple Delivery of Multiple Reagents for Multistep Assays. 2016 [cited 2021 Sep 18];Available from: https://pubs.acs.org/sharingguidelines

35. Li B, Yu L, Qi J, Fu L, Zhang P, Chen L. Controlling Capillary-Driven Fluid Transport in Paper-Based Microfluidic Devices Using a Movable Valve. Analytical Chemistry [Internet] 2017 [cited 2021 Sep 17];89(11):5707–12. Available from: https://pubs.acs.org/doi/full/10.1021/acs.analchem.7b00726

36. Liu M, Wu J, Gan Y, Hanaor DAH, Chen CQ. Combining geometrical and evaporation effects. International Journal of Heat and Mass Transfer [Internet] 2018 [cited 2021 Sep 17];123. Available from: https://hal.archives-ouvertes.fr/hal-02345595

37. Liu Z, Hu J, Zhao Y, Qu Z, Xu F. Experimental and numerical studies on liquid wicking into filter papers for paper-based diagnostics. Applied Thermal Engineering 2015;88:280–7.

38. Liu M, Wu J, Gan Y, Hanaor DAH, Chen CQ. Evaporation Limited Radial Capillary Penetration in Porous Media. Langmuir [Internet] 2016 [cited 2021 Sep 17];32(38):9899–904. Available from: https://pubs.acs.org/doi/full/10.1021/acs.langmuir.6b02404

39. Conrath M, Fries N, Zhang M, Dreyer ME, Conrath M, Fries · N, et al. Radial Capillary Transport from an Infinite Reservoir. Transp Porous Med 2010;84:109–32.

40. Madhu NT, E RP, Pradeep A, Satheesh Babu TG. Design and simulation of fluid flow in paper based microfluidic platforms.

41. Patari S, Mahapatra PS. Liquid wicking in a paper strip: An experimental and numerical study. ACS Omega [Internet] 2020 [cited 2021 Jun 4];5(36):22931–9. Available from: /pmc/articles/PMC7495729/

42. ben Neriah A, Assouline S, Shavit U, Weisbrod N. Impact of ambient conditions on evaporation from porous media. Water Resources Research [Internet] 2014 [cited 2021 Jun 8];50(8):6696–712. Available from: https://agupubs.onlinelibrary.wiley.com/doi/full/10.1002/2014WR015523

43. Deegan RD, Bakajin O, Dupont TF, Huber G, Nagel SR, Witten TA. Contact line deposits in an evaporating drop. Physical Review E - Statistical Physics, Plasmas, Fluids, and Related Interdisciplinary Topics [Internet] 2000 [cited 2021 Jun 8];62(1 B):756–65. Available from: https://journals.aps.org/pre/abstract/10.1103/PhysRevE.62.756

44. Modeling and analysis of evaporation processes from porous media on the REV scale [Internet]. [cited 2021 May 31];Available from: https://agupubs.onlinelibrary.wiley.com/doi/epdf/10.1002/2013WR014442

45. Evaporation rates across a convective air boundary layer are dominated by diffusion [Internet]. [cited 2021 May 31];Available from: https://agupubs.onlinelibrary.wiley.com/doi/epdf/10.1002/wrcr.20166

46. Modha S, Castro C, Tsutsui H. Recent developments in flow modeling and fluid control for paper-based microfluidic biosensors. Biosensors and Bioelectronics 2021;178:113026.

47. Shin JH, Park J, Kim SH, Park JK. Programmed sample delivery on a pressurized paper. Biomicrofluidics [Internet] 2014 [cited 2021 May 31];8(5):54121. Available from: https://doi.org/10.1063/1.48997738,054121

48. Rivas L, Medina-Sánchez M, de La Escosura-Muñiz A, Merkoçi A. Improving sensitivity of gold nanoparticle-based lateral flow assays by using wax-printed pillars as delay barriers of microfluidics. Lab on a Chip [Internet] 2014 [cited 2021 May 31];14(22):4406–14. Available from: www.rsc.org/loc

49. Zhang Y, Odiwuor N, Xiong J, Sun L, Nyaruaba RO, Wei H, et al. Rapid Molecular Detection of SARS-CoV-2 (COVID-19) Virus RNA Using Colorimetric LAMP. medRxiv [Internet] 2020 [cited 2021 Jun 2];2020.02.26.20028373. Available from: https://doi.org/10.1101/2020.02.26.20028373

50. Wang S, Ge L, Song X, Yu J, Ge S, Huang J, et al. Paper-based chemiluminescence ELISA: Lab-on-paper based on chitosan modified paper device and wax-screen-printing. Biosensors and Bioelectronics 2012;31(1):212–8.

51. Chan SK, Lim TS. A straw-housed paper-based colorimetric antibody-antigen sensor. Analytical Methods [Internet] 2016 [cited 2021 Jun 2];8(6):1431–6. Available from: www.rsc.org/methods

52. Ma L, Nilghaz A, Choi JR, Liu X, Lu X. Rapid detection of clenbuterol in milk using microfluidic paper-based ELISA. Food Chemistry 2018;246:437–41.